ORIGINAL ARTICLE

Journal Section

Adaptively Implicit MPDATA Advection for Arbitrary Courant numbers and Meshes

Hilary Weller, PhD[1] | James Woodfield MRes[2] | Christian Kühnlein[3] | Piotr K. Smolarkiewicz[4]

[1]Meteorology, University of Reading, RG6 6BB, UK

[2]Mathematics, University of Reading, RG6 6BB, UK

[3]ECMWR, 53175 Bonn, Germany

[4]NCAR, Boulder, CO 80307-3000, USA

Correspondence
Hilary Weller, Meteorology, University of Reading, RG6 6BB, UK
Email: h.weller@reading.ac.uk

Funding information

Advection schemes with time step restrictions are widely used in weather and climate models. This can lead to instability in the presence of high flow speeds (relative to mesh spacing) such as occurs in convective updrafts, regions of mesh convergence or where the winds are unusually high. An adaptively implicit advection scheme is proposed which treats advection implicitly only where the Courant number is high. Flux-correction to ensure monotonicity is adapted to work with implicit time stepping.

A version of MPDATA (Multidimensional Positive Definite Advection Transport Algorithm) is derived with an anti-diffusive flux to correct off-centred implicit time stepping. The anti-diffusive flux is gradually reduced as Courant numbers increase above 2 in order to maintain stability at the expense of second-order accuracy at high Courant numbers.

Results of two-dimensional advection by deformational flow are presented on various meshes of the sphere. Stability and second-order accuracy are maintained when the Courant number is over 100 in a small region, when strong wind crosses the poles of a rotated latitude-longitude mesh. Good solutions are also obtained on a skipped latitude-longitude mesh, a cubed sphere and hexagonal meshes. Accuracy reverts to first-order when Courant numbers are large over a large fraction of the domain.

KEYWORDS
Advection, Transport, Courant number, implicit, monotonicity, stable

Contents

1 | INTRODUCTION

1.1 | Motivation

Time step restrictions based on advection have always posed a problem for models of the atmosphere. The Courant-Friedrichs-Lewy (CFL) condition states that explicit Eulerian advection schemes will have time step restrictions based on the size of the spatial discretisation increments and the flow speed. Typically this means that explicit schemes cannot run with a Courant number greater than one or thereabouts. This is equivalent to saying that an advected quantity cannot be moved by more than one mesh cell (or grid box) in one time step.

CFL constraints can be particularly cruel where spatial resolution is higher than it needs to be for accuracy, such as near the poles of a latitude-longitude mesh. An early workaround was to use polar filtering; artificially removing oscillations near the poles where mesh lines converge (Cullen and Davies, 1991). However polar filtering led to parallel scaling bottlenecks and mistrust of solutions near the poles in models of the atmosphere. The UK Met Office gained accuracy and efficiency by replacing their model employing polar filtering with a semi-implicit , semi-Lagrangian (SISL) model to avoid time step restrictions on a latitude-longitude mesh (Davies et al., 2005). SISL eases time step constraints by treating acoustic and gravity waves implicitly while the advection is solved with the semi-Lagrangian method which is stable, accurate for smooth flows and efficient with long time steps, but not conservative. The lack of conservation is regarded as inadequate for climate modelling and is associated with spurious features such as eternal fountains which involve a positive feedback loop that creates moisture in convectively unstable columns (Zerroukat and Allen, 2020).

The requirement to run stably with large Courant numbers is less severe now that models of the global atmosphere have largely moved away from latitude-longitude meshes in favour of quasi-uniform meshes such as the cubed sphere and icosahedral meshes (Ullrich et al., 2017). However, the problem remains severe in the vertical direction where mesh spacing can be fine and large vertical velocities can occur when atmospheric convection is resolved. A solution in the vertical direction is to use Lagrangian floating levels (Lin, 2004) that are conservatively mapped back to the fixed Eulerian mesh. The Lagrangian floating levels technique is equivalent to conservative semi-Lagrangian (Harris et al., 2011), and can be made efficient for large Courant numbers in one dimension and consequently can work on tensor product meshes (eg. Leonard et al., 1996). Conservative, flux-form semi-Lagrangian schemes have been developed for arbitrary meshes (eg. Miura, 2007) but only work efficiently for large Courant numbers on tensor-product grids. Conservative semi-Lagrangian is related to the Arbitrary Lagrangian-Eulerian (ALE) method (eg. Hirt et al., 1997) which solves equations in a Lagrangian frame and then remaps the solution back to the original mesh. However ALE methods suffer from time step restrictions associated with avoiding mesh tangling.

Due to the difficulties in allowing long time steps while maintaining exact local conservation on arbitrary meshes, it is worth considering implicit time stepping for advection. The aim of this paper is to present an advection scheme with the following properties:

1. stable for large Courant numbers;
2. applicable on arbitrary meshes;
3. locally conservative to machine precision;
4. similar cost and accuracy to explicit schemes when the Courant number is below one;
5. at least first-order accurate where the Courant number is large;
6. options to be monotonic, bounded or sign preserving;
7. multi-tracer efficient;
8. good parallel scaling.

We define a bounded advection scheme as one that does not produce solution values outside specified bounds, for example $[0,1]$. MPDATA (Multidimensional Positive Definite Advection Transport Algorithm) is sign preserving (positive definite) which means solutions that start in $[0,\infty)$ stay in $[0,\infty)$. A monotonic advection scheme does not generate new spurious extrema or amplify existing extrema. This is desirable as it implies boundedness and also guarantees stability.

This paper proposes the use of adaptively implicit time stepping combined with MPDATA to create a scheme with options to be monotonic, bounded, positive definite or just stable for all Courant numbers. The methods for combining

implicit and explicit and the method for achieving monotonicity should translate to other explicit advection schemes.

1.2 | Background on MPDATA

The MPDATA scheme for the solution of the advection equation was introduced by Smolarkiewicz (1983, 1984). The basic principle of MPDATA is as follows: apply the forward in time, first-order upwind scheme based on the physical flow velocity, followed by a corrective upwind step with a pseudo-velocity that is designed to compensate the spatial and temporal truncation errors of the preceding step to at least second order. Due to the repeated application of the upwind scheme, MPDATA provides strict sign preservation of the transported field and a small phase error. The standard MPDATA is an explicit flux-form Eulerian scheme and stable for an advective Courant number less than one. Various MPDATA extensions including some for entire flow solvers have been developed over the years. Smolarkiewicz and Margolin (1998) review the schemes with a focus on structured grids.

MPDATA options of particular interest to the current paper are the infinite-gauge variant for the transport of signed quantities (Smolarkiewicz and Clark, 1986) and the extension to enforce solution monotonicity (Smolarkiewicz and Grabowski, 1990) by means of flux-corrected transport (FCT, Zalesak, 1979). Smolarkiewicz and Szmelter (2005) extended MPDATA to fully unstructured meshes while retaining second-order accuracy and the other favourable properties of the scheme. Kühnlein and Smolarkiewicz (2017) formulate the MPDATA pseudo-velocity based solely on face-normal fluxes which facilitated integration of compressible PDEs on arbitrary unstructured meshes. While the standard MPDATA scheme is fully multidimensional, Kühnlein et al. (2019) use a horizontal-vertical second-order accurate Strang-split integration based on MPDATA that permits larger time steps and also enables more targeted schemes in the different coordinate directions of the global atmospheric model.

1.3 | Background on Implicit Advection Schemes

Implicit time stepping is ubiquitous in atmospheric modelling for solving the terms of the equations of motion responsible for fast waves such as gravity and acoustic waves. However, implicit time stepping has rarely been used for advection in atmosphere and ocean modelling. Implicit time stepping for advection in the mathematics and engineering literature will be discussed first and then we will return to its uses to date in atmosphere and ocean modelling.

Implicit time stepping for advection has a severe order barrier; no implicit method exists with order greater than one which is monotonic for all time steps (Gottlieb et al., 2001). Higher order implicit multi-stage (Runge-Kutta) and multi-step schemes exist that are unconditionally linearly stable but if we additionally require monotonicity (no new spurious extrema generated), then higher-order implicit methods have time step restrictions, known as radii of monotonicity. As with spatial discretisation, high order implicit time stepping has been non-linearly combined with first order implicit time stepping to try to break the order barrier and increase the radius of monotoncity. Yee et al. (1985); Yee (1987) proposed implicit TVD (total variation diminishing) schemes for solving hyperbolic equations and achieved high accuracy for large Courant numbers. However they could not find a second-order scheme that was guaranteed both TVD and conservative for non-constant coefficient advection. May and Berger (2017) used FCT (Zalesak, 1979) to improve temporal accuracy in implicitly solved small cells without generating new extrema.

In atmospheric modelling, implicit time stepping for advection has been used for vertical advection (Baldauf et al., 2011) and to treat small, cut-cells stably at modest time steps (e.g. Jebens et al., 2011). Wicker and Skamarock (2020); Li and Zhang (2022) use adaptively implicit vertical transport to treat isolated strong updrafts stably, avoiding the order barrier by limiting order of accuracy to first (upwind) where ever implicit time stepping is used. The lack of accuracy was not considered problematic because of the sparsity of the use of implicit advection, although Li and Zhang (2022)

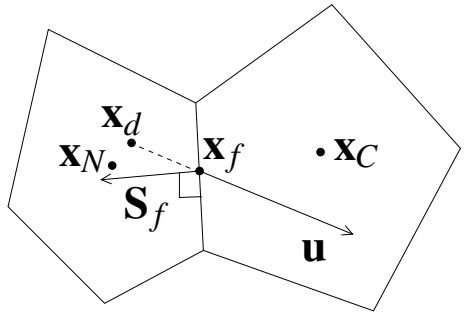

FIGURE 1 Two cells in an arbitrary mesh. $\mathbf{x}_C$ and $\mathbf{x}_N$ are the cell centres (centroids) of cell C and its neighbour, N, over face f and $\mathbf{x}_f$ is the face centre. $\mathbf{S}_f$ is the face area vector, normal to face f with magnitude equal to the face area. $\mathbf{u}$ is the velocity and $\mathbf{x}_d$ is the departure point for face f at $t^{n+\frac{1}{2}}$ (i.e. the centre of the volume swept through the face between t^n and t^{n+1}).

describe the implicit advection as being more diffusive than explicit advection. Chen et al. (2017) compared implicit advection with dimensionally split, flux-form semi-Lagrangian advection and found that the dimensionally split scheme was more accurate and more efficient than implicit advection for all Courant numbers. However, this was not a like for like comparison; the dimensionally split scheme was a higher-order accurate scheme, limited to tensor product meshes and suffered from mesh imprinting errors on distorted meshes.

1.4 | Outline

The description of the adaptively implicit MPDATA in section 2 starts with an alternative formulation of the standard explicit MPDATA on an unstructured, centroidal mesh, without co-ordinate transforms. This description is then extended to the implicit case including a description of how the explicit and implicit schemes are blended to ensure efficiency and stable solutions, how the infinite gauge variant is used with the implicit scheme and how FCT can be used with an implicit scheme. The description is general for one, two and three dimensions but, in this paper, does not include the terms for divergent velocity fields. The numerical results in section 3 start in one dimension, comparing an explicit scheme on a uniform grid with an adaptively implicit scheme on a non-uniform grid. The remainder of the results are of deformational flow on the surface of the sphere, demonstrating convergence and monotonicity for a wide range of Courant numbers. The adaptively implicit time stepping with first-order spatial discretisation is proved to be bounded in Appendix A and a one-dimensional version of the adaptively implicit scheme is proved to be stable for all Courant numbers in Appendix B.

2 | AN ADAPTIVELY IMPLICIT MPDATA

The version of explicit MPDATA and the adaptively implicit MPDATA defined here are implemented using the OpenFOAM library (`https://openfoam.org/`) using standard OpenFOAM operators and linear equation solvers. The code is available as part of the AtmosFOAM repository (`https://github.com/AtmosFOAM/`) compiled with OpenFOAM7.

2.1 | Explicit MPDATA on an Arbitrary Mesh

The description of the explicit scheme is consistent with basic MPDATA principles (e.g. Smolarkiewicz and Szmelter, 2005), but introduces a novel derivation based on a flux-form semi-Lagrangian method and assuming an arbitrary, centroidal mesh in Cartesian co-ordinates rather than using co-ordinate transforms. We will describe MPDATA for solving the linear advection equation for advected quantity ψ with velocity field $\mathbf{u}$:

$$\frac{\partial \psi}{\partial t} + \nabla \cdot (\mathbf{u}\psi) = 0. \tag{1}$$

This is solved using Gauss's divergence theorem on an arbitrary mesh to go from time t^n to t^{n+1} a time step Δt apart:

$$\psi_c^{n+1} = \psi_c^n - \frac{\Delta t}{\mathscr{V}_c} \sum_{f \in C} \psi_f^{n+\frac{1}{2}} U_f, \tag{2}$$

where ψ_c is the cell mean value of ψ in cell C, $\mathscr{V}_c$ is the volume of cell C, $f \in C$ are the faces of cell C, $\psi_f^{n+\frac{1}{2}}$ is the value of ψ at face f at $t^{n+\frac{1}{2}}$, $\mathbf{u}_f$ the velocity at face f and $\mathbf{S}_f$ is the face area vector — the outward pointing vector normal to face f with magnitude equal to the area of face f (Fig. 1). $U_f = \mathbf{u}_f \cdot \mathbf{S}_f$ is the volume flux over face f. In this derivation of MPDATA, ψ_f is evaluated at the departure point of the face centre at t^n. The departure point, $\mathbf{x}_d$, is the centre of the volume swept through the face between t^n and t^{n+1} which is approximated by the point a distance $\mathbf{u}\Delta t 2$ upstream of the face centre:

$$\mathbf{x}_d = \mathbf{x}_f - \frac{\Delta t}{2}\mathbf{u}_f + O\left(\Delta t\right)^2, \tag{3}$$

where $\mathbf{x}_f$ is the face centre (see Fig. 1). The velocity, $\mathbf{u}_f$, is evaluated at $t^{n+\frac{1}{2}}$ at the face centre. In this paper, we consider passive advection of ψ with a prescribed non-divergent wind field. In a dynamical model, $\mathbf{u}_f^{n+\frac{1}{2}}$ would be evaluated from velocities at known positions and times.

The dependent variable, ψ, is evaluated at the departure point, $\mathbf{x}_d$, using the upwind cell centre value of ψ, the gradient of ψ at the face centre and the velocity divergence at the face centre (assumed zero):

$$\psi_f^{n+\frac{1}{2}} = \psi_d^n = \psi_{\text{up}}^n + \left(\mathbf{x}_d - \mathbf{x}_{\text{up}}\right) \cdot \nabla \psi^n - \frac{\Delta t}{2} \psi_{\text{up}}^n \cancelto{0}{\nabla \cdot \mathbf{u}} + O\left(\Delta s^2, \Delta t^2\right), \tag{4}$$

where ψ_{up} is the value of ψ in the cell upwind of face f, Δs is the cell centre to cell centre distance, $\mathbf{x}_{\text{up}}$ is the location of the upwind cell centre and $\mathbf{x}_{\text{down}}$ is the location of the downwind cell centre (which will be used later). Eqns. (3) and (4) are substituted in to (2) to give a scheme that is second-order accurate in space and time but not sign preserving, equivalent to a Lax-Wendroff scheme:

$$\begin{aligned} \psi_c^{n+1} \quad = \quad & \psi_c^n - \underbrace{\frac{\Delta t}{\mathscr{V}_c} \sum_{f \in C} \psi_{\text{up}}^n U_f}_{\text{explicit upwind}} - \underbrace{\frac{\Delta t}{\mathscr{V}_c} \sum_{f \in C} \left(\mathbf{x}_f - \mathbf{x}_{\text{up}}\right) \cdot \nabla \psi^n U_f}_{\text{spatial correction}} + \underbrace{\frac{\Delta t^2}{2\mathscr{V}_c} \sum_{f \in C} \mathbf{u}_f \cdot \left(\nabla \psi^n\right)_f U_f}_{\text{temporal correction}} \\ + \quad & \Delta t \; O\left(\Delta s^2, \Delta t^2\right). \end{aligned} \tag{5}$$

The explicit upwind scheme is monotone. In order for the spatial and temporal correction terms to be sign-preserving, they are written as explicit upwind advection using an anti-diffusive flux, $V_f = \mathbf{v}_f \cdot \mathbf{S}_f$. The anti-diffusive flux is divergent so new extrema are not prevented. The use of the anti-diffusive flux transforms the scheme from Lax-Wendroff to

MPDATA and is written in two stages:

$$\text{explicit upwind step: } \psi_c^1 = \psi_c^n - \frac{\Delta t}{\mathscr{V}_c} \sum_{f \in C} \psi_{\text{up}}^n U_f, \tag{6}$$

$$\text{explicit correction: } \psi_c^{n+1} = \psi_c^1 - \frac{\Delta t}{\mathscr{V}_c} \sum_{f \in C} \psi_{\text{vup}}^1 V_f, \tag{7}$$

$$\text{where } V_f = \mathbf{v}_f \cdot \mathbf{S}_f = \frac{U_f}{\psi} \left\{ \left(\mathbf{x}_f - \mathbf{x}_{\text{up}}\right) \cdot \nabla\psi - \frac{\Delta t}{2} \mathbf{u}_f \cdot \left(\nabla\psi\right)_f \right\}, \tag{8}$$

and where ψ_{vup} is ψ in the upwind cell where the upwind direction is defined by the sign of V_f. As ψ is always positive, there is no ambiguity in the sign of V_f. The anti-diffusive flux, V_f, can be calculated iteratively, using first ψ^1 and subsequent iterations use the most up to date version of ψ^{n+1} and V_f. All simulations in this paper use one iteration per time step. Eqn (8) is a continuous version of the expression for the anti-diffusive velocity in eqn (13) of Smolarkiewicz and Szmelter (2005). The discretisation of gradients and divergences described here are similar to those of Smolarkiewicz and Szmelter (2005).

The first term of (8) is discretised by assuming that $\mathbf{x}_f - \mathbf{x}_{\text{up}} = \frac{1}{2}\left(\mathbf{x}_{\text{down}} - \mathbf{x}_{\text{up}}\right)$ and preventing division by zero:

$$\frac{\left(\mathbf{x}_f - \mathbf{x}_{\text{up}}\right) \cdot \nabla\psi}{\psi} \approx \frac{\psi_{\text{down}} - \psi_{\text{up}}}{\psi_{\text{down}} + \psi_{\text{up}} + \varepsilon}, \tag{9}$$

which is second-order accurate only on non-skew, uniform grids. The results presented in section 3 use $\varepsilon = 10^{-16}$. The second term of (8) is discretised using a second-order, least-squares approximation for $\nabla\psi$ in cells:

$$\nabla\psi = \sum_{f \in C} \mathbf{g}_f \left(\psi_N - \psi_c\right), \tag{10}$$

where ψ_N is ψ in the neighbour of cell C across face f and where $\mathbf{g}_f$ is a vector calculated for each face of cell C based entirely on the local mesh geometry:

$$\mathbf{g}_f = \left(1 - w_f\right) \frac{|\mathbf{S}_f|}{|\mathbf{x}_N - \mathbf{x}_C|^2} D_C^{-1} \left(\mathbf{x}_N - \mathbf{x}_C\right), \tag{11}$$

$$\text{where } w_f = \frac{|\mathbf{S}_f \cdot \mathbf{x}_N - \mathbf{x}_f|}{|\mathbf{S}_f \cdot \mathbf{x}_N - \mathbf{x}_f| + |\mathbf{S}_f \cdot \mathbf{x}_f - \mathbf{x}_C|} \text{ (interpolation weights)}$$

$$\text{where } D_C = \sum_{f \in C} \left(1 - w_f\right) \frac{|\mathbf{S}_f|}{|\mathbf{x}_N - \mathbf{x}_C|^2} \left(\mathbf{x}_N - \mathbf{x}_C\right) \left(\mathbf{x}_N - \mathbf{x}_C\right)^T.$$

This is the least squares gradient implemented in the OpenFOAM library. Cell centre gradients are then linearly interpolated onto face centres, denoted $\left(\nabla\psi\right)_f$. The component in the $\mathbf{x}_N - \mathbf{x}_C$ direction is corrected using the compact gradient:

$$\left(\nabla\psi\right)_f \cdot \left(\mathbf{x}_N - \mathbf{x}_C\right) = \psi_N - \psi_c. \tag{12}$$

2.1.1 | Sign Preservation

Given the definition of the Courant number on an arbitrary mesh,

$$c = \frac{1}{2} \sum_f \frac{\Delta t}{\mathscr{V}_c} |U_f|, \tag{13}$$

Smolarkiewicz and Szmelter (2005) showed that explicit upwind is monotonic for non-divergent velocity fields when $c \leq 1$ and sign preserving for a divergent velocity field when $c \leq 12$. The anti-diffusive velocity is divergent so the Courant number based on the anti-diffusive velocity must be less than 12 for the explicit MPDATA to be sign preserving. Smolarkiewicz and Szmelter (2005) showed that the median-dual MPDATA discretisation of the anti-diffusive flux satisfies this criterion for $c \in 0, 1$. In order to guarantee sign preservation in this paper, we limit the anti-diffusive flux so that

$$|V_f U_f| \leq \frac{1}{2}. \tag{14}$$

For the tests presented in section 3, the anti-diffusive fluxes satisfied (14) without limiting, but we have not (yet) proven if this will always hold.

2.2 | Adaptively Implicit MPDATA

The adaptively implicit scheme is a generalisation of Crank-Nicolson with off-centering θ which can vary in space. θ_f is defined on faces (for conservation) so the time stepping is defined as:

$$\psi_c^{n+1} = \psi_c^n - \frac{\Delta t}{\mathscr{V}_c} \sum_{f \in C} \left\{ \left(1 - \theta_f\right) \psi_f^n + \theta_f \psi_f^{n+1} \right\} U_f. \tag{15}$$

This is second order in time only for $\theta_f = \frac{1}{2}$ globally. We will next derive the MPDATA anti-diffusive flux that corrects a scheme which is first-order accurate in space and off-centered by θ in time. So the first step, before the MPDATA correction, is:

$$\psi_c^1 = \psi_c^n - \frac{\Delta t}{\mathscr{V}_c} \sum_{f \in C} \left\{ \left(1 - \theta_f\right) \psi_{\mathrm{up}}^n + \theta_f \psi_{\mathrm{up}}^1 \right\} U_f. \tag{16}$$

The proof that this first step gives positive, bounded and hence stable solutions for non-divergent velocity fields on arbitrary meshes is provided in Appendix A.

To find the second-order approximation of ψ_f^{n+12} for non-divergent flow, we consider a linear combination of ψ at the departure point at t^n and ψ at the arrival point at t^{n+1}:

$$\psi_f^{n+12} = \left(1 - \theta_f\right) \psi_d^n + \theta_f \psi_a^{n+1}, \tag{17}$$

where the locations of the departure and arrival points are shown in Fig. 2 and are given by

$$\begin{aligned} \mathbf{x}_d &= \mathbf{x}_f - \frac{\Delta t}{2} \mathbf{u}_f, \\ \mathbf{x}_a &= \mathbf{x}_f + \frac{\Delta t}{2} \mathbf{u}_f. \end{aligned}$$

The values of ψ at the departure and arrival points can be approximated by

$$\begin{aligned} \psi_d^n &= \psi_{\mathrm{up}}^n + \left(\mathbf{x}_d - \mathbf{x}_{\mathrm{up}}\right) \cdot \nabla \psi, \\ \psi_a^{n+1} &= \psi_{\mathrm{up}}^{n+1} + \left(\mathbf{x}_a - \mathbf{x}_{\mathrm{up}}\right) \cdot \nabla \psi. \end{aligned}$$

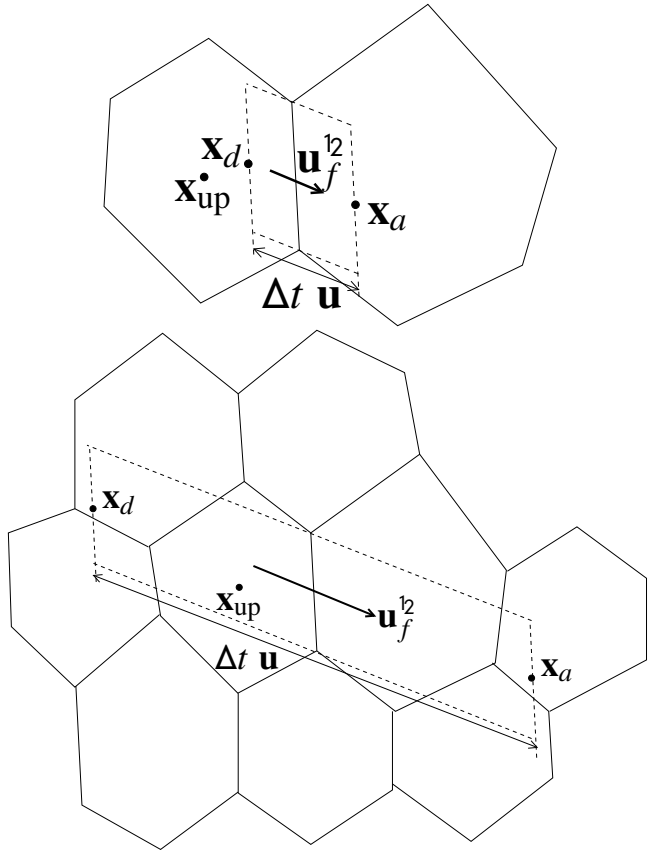

FIGURE 2 The volume that is swept through face f in one time step and the departure and arrival points, $\mathbf{x}_d$ and $\mathbf{x}_a$ for small (left) and large (right) Courant numbers.

Substituting these into (17) gives

$$\psi_f^{n+\frac{1}{2}} = \left(1-\theta_f\right)\psi_{\mathsf{up}}^{n} + \theta_f\psi_{\mathsf{up}}^{n+1} + \left(\mathbf{x}_f - \mathbf{x}_{\mathsf{up}}\right)\cdot\nabla\psi^{n} - \left(1-2\theta_f\right)\frac{\Delta t}{2}\mathbf{u}\cdot\nabla\psi, \tag{18}$$

where $\mathbf{x}_{\mathsf{up}}$ is the centre of the cell upwind of face f. This correction is not stable for Courant number, $c > 2$ or $\theta > \frac{1}{2}$ (Appendix (B)). For stability for all c and second-order accuracy where $\theta \leq \frac{1}{2}$ the correction step is:

$$\psi_c^{n+1} = \psi_c^{1} + \frac{\Delta t}{\mathscr{V}_c}\sum_{f\in C}\psi_{\mathsf{vup}}^{1}V_f, \tag{19}$$

$$\text{where } V_f = \mathbf{v}_f\cdot\mathbf{S}_f = \frac{U_f}{\psi}\left\{\left(\mathbf{x}_f - \mathbf{x}_{\mathsf{up}}\right)\cdot\nabla\psi - \chi\frac{\Delta t}{2}\mathbf{u}\cdot\nabla\psi\right\}, \tag{20}$$

$$\chi = \max\left(1-2\theta_f,\, 0\right), \tag{21}$$

where spatial discretisation is as in section 2.1. Eqn. (21) gives a first-order error in time for $\theta > \frac{1}{2}$ which is only used for large Courant numbers (> 2). It is stable on a uniform one-dimensional grid (Appendix (B)) but on an arbitrary mesh, some smoothing is needed when $\theta > 0$ (section 2.2.1).

Appendix (B) shows that the first (diffusive) step of the adaptively implicit MPDATA scheme, Eqn. (16), is stable and bounded when

$$\theta \geq \max\left(1-\frac{1}{c},\, 0\right), \tag{22}$$

with the Courant number for an arbitrary mesh, c, defined as in (13). Eqn. (22) can be used to set θ_f based on the values of the Courant number in the cells either side, c_{up} and c_{down} with a degree of safety added to avoid reaching the stability limits:

$$\theta_f = \max\left\{1-\frac{1}{c_{\mathsf{up}}+0.25},\, 1-\frac{1}{c_{\mathsf{down}}+0.25},\, 0\right\}. \tag{23}$$

2.2.1 | Additional Smoothing for Large Courant numbers

Appendix B shows that a linearised version of the adaptively implicit MPDATA is unconditionally stable on a uniform, one-dimensional grid. However this does not carry over onto an arbitrary mesh. Therefore V_f is smoothed where $\theta > 0$. First a cell centre anti-diffusive flux is reconstructed from surrounding fluxes:

$$\mathbf{v}_c = \left(\sum_{f\in C}\mathbf{S}_f\mathbf{S}_f^T\right)^{-1}\sum_{f\in C}\mathbf{S}_f V_f, \tag{24}$$

which is the standard reconstruction of vectors from fluxes implemented in OpenFOAM; $\sum_{f\in C}\mathbf{S}_f\mathbf{S}_f^T$ is a tensor which can be inverted and pre-calculated for each cell. This is a second-order accurate, least squares reconstruction which reconstructs a uniform vector field exactly. The reconstructed velocity is then interpolated back onto faces and the dot product taken with $\mathbf{S}_f$ to get a smoothed flux. The smoothed flux is used for faces with $\theta_f > 0$ and for all faces of

a cell if that cell has one face with $\theta_f > 0$:

$$V_f = \begin{cases} V_f \text{ from 20} & \text{if } \theta_f = 0 \text{ and } \theta_{f'} = 0 \; \forall \; f' \in C,N \text{ of } f \\ \mathbf{v}_{cf} \cdot \mathbf{S}_f & \text{otherwise,} \end{cases} \tag{25}$$

where $\mathbf{v}_{cf}$ is the reconstructed velocity $\mathbf{v}_c$ linearly interpolated from cell centres to faces. The notation $\forall \; f' \in C,N$ of f means for all faces f' which are faces of cells C and N which are the cells surrounding face f.

2.3 | Linear Equation Solver

The first-order upwind adaptively implicit advection creates a sparse, asymmetric matrix M with positive elements on the diagonal. To create the matrix equation, (16) is re-arranged so that the vector of new ψ^1 values ($\underline{\psi}^1$) is a linear combination of old ψ^n values ($\underline{\psi}^n$):

$$M\underline{\psi}^1 = N\underline{\psi}^n, \tag{26}$$

$$\text{where } M_{ij} = \begin{cases} 1 + \frac{\Delta t}{V_i} \sum_{f \in i} \theta_f \max\left\{U_f, 0\right\} & \text{for } i = j \\ -\frac{\Delta t}{V_i} \theta_f \max\left\{-U_f, 0\right\} & \text{where } f \text{ is between cells } i \text{ and } j \end{cases} \tag{27}$$

$$\text{and } N_{ij} = \begin{cases} 1 - \frac{\Delta t}{V_i} \sum_{f \in i} \left(1 - \theta_f\right) \max\left\{U_f, 0\right\} & \text{for } i = j \\ +\frac{\Delta t}{V_i} \left(1 - \theta_f\right) \max\left\{-U_f, 0\right\} & \text{where } f \text{ is between cells } i \text{ and } j. \end{cases} \tag{28}$$

Matrix N is of course not created because the R.H.S. vector entries can be evaluated directly. If the flow is non-divergent then $\sum_{f \in i} U_f = 0$ which implies that M is strictly diagonally dominant. Note that M has no off diagonal elements where the time stepping is explicit. M will not be diagonally dominant at row i if the volume flux into cell i in one time step is greater than the volume flux out in that time step plus the cell volume. This situation is not likely for atmospheric modelling as the atmosphere is low Mach number but it would require either a smaller time step or a matrix solver suitable for non-diagonally dominant matrices.

The resulting linear equation system is solved with the standard OpenFOAM bi-conjugate gradient solver with a diagonal incomplete LU preconditioner (DILU). Solver tolerance and iteration counts are discussed in section 3.4.

2.4 | Infinite Gauge MPDATA

The infinite gauge variant of MPDATA (a realisation of Lax-Wendroff) can be used with the adaptively implicit time stepping exactly as it is used with standard, explicit MPDATA (Smolarkiewicz and Clark, 1986; Kühnlein and Smolarkiewicz, 2017). This removes the non-linearity of MPDATA and means that MPDATA is no longer sign preserving, but monotone solutions can be achieved using FCT, as described below.

2.5 | Flux-Corrected Transport (FCT) with Implicit Time Stepping

Zalesak (1979) state that FCT can be used with implicit time stepping although we have not found examples of this in the literature. In fact, the algorithm as described by Zalesak (1979) does not guarantee monotonicity when used with implicit time stepping. This is because Zalesak (1979) bound the tracer at t^{n+1} by the diffusively transported tracer at t^{n+1} and the tracer at t^n at the current and upwind grid points. The tracer at t^n at the current and upwind grid points are

not a suitable bounds if the tracer can move a long distance in one time step. When using implicit time stepping and large Courant numbers, local extrema can be advected by more than one mesh cell in one time step so local bounds from the previous time step no longer apply. We therefore define two variants of FCT to work with implicit time stepping. One guarantees monotonicity and the other guarantees global boundedness given user defined bounds.

The first step of FCT is to advect using a monotonic, diffusive scheme to calculate ψ^1. Appendix A shows that the first-order upwind in space, adaptively implicit in time scheme (Eqn. 16) provides this solution for arbitrary Courant numbers. The next step is to calculate the allowable minima and maxima for each cell which we will call $\psi_{\min}$ and $\psi_{\max}$. If we seek boundedness within pre-defined bounds then $\psi_{\min}$ and $\psi_{\max}$ are these bounds. Otherwise $\psi_{\min}$ and $\psi_{\max}$ are the local extrema of ψ^1 in the current and neighbouring cells. Explicit FCT also uses ψ^n which widens the bounds. Consequently, FCT for implicit, monotonic advection will be more diffusive because of the use solely of ψ^1 to define the local bounds:

$$\text{for cell } C \ \psi_{\min} = \min_{N \in C} \left\{ \psi_N^1 \right\} \text{ where } N \text{ are the face neighbours of } C, \tag{29}$$

$$\text{for cell } C \ \psi_{\max} = \max_{N \in C} \left\{ \psi_N^1 \right\} \text{ where } N \text{ are the face neighbours of } C. \tag{30}$$

We next define the maximum allowable amount that each cell can rise or fall by and use the same notation as Zalesak (1979)

$$Q_p = \psi_{\max} - \psi^1, \tag{31}$$

$$Q_m = \psi^1 - \psi_{\min}. \tag{32}$$

We next need to modify the non-monotonic MPDATA high order flux corrections (HOC). The HOC is the MPDATA flux correction, V_f, from (25) multiplied by ψ^1 at the upwind cell (upwind defined relative to V_f):

$$F_{f\mathsf{HOC}} = \psi^1_{\mathsf{up}} V_f. \tag{33}$$

From this we calculate the total high order flux that enters (P_p) and leaves (P_m) each cell:

$$P_p = -\frac{\Delta t}{\mathscr{V}_c} \sum_{f \in C} \min \left\{ F_{f\mathsf{HOC}}, \, 0 \right\}, \tag{34}$$

$$P_m = \frac{\Delta t}{\mathscr{V}_c} \sum_{f \in C} \max \left\{ F_{f\mathsf{HOC}}, \, 0 \right\}. \tag{35}$$

Next we find the ratios of the allowable total fluxes to the actual high order fluxes:

$$R_p = \begin{cases} \min \left\{ 1, \, \frac{Q_p}{P_p} \right\} & \text{if } P_p > 0 \\ 0 & \text{otherwise} \end{cases} \tag{36}$$

$$R_m = \begin{cases} \min \left\{ 1, \, \frac{Q_m}{P_m} \right\} & \text{if } P_m > 0 \\ 0 & \text{otherwise.} \end{cases} \tag{37}$$

Finally we find the coefficient to multiply $F_{f\mathsf{HOC}}$ in order to achieve either a monotonic solution or a solution with the

required bounds:

$$\begin{aligned} F_f &= \begin{cases} F_{f\text{HOC}} \min\left\{R_{pN},\, R_{mC}\right\} & \text{if } F_{f\text{HOC}} \geq 0 \\ F_{f\text{HOC}} \min\left\{R_{pC},\, R_{mN}\right\} & \text{otherwise,} \end{cases} \\ \text{where} \quad & \left(\mathbf{x}_N - \mathbf{x}_C\right) \cdot \mathbf{S}_f > 0, \end{aligned}$$

and cells C and N are either side of face f. Then the final update is

$$\psi_c^{n+1} = \psi_c^1 - \frac{\Delta t}{\mathscr{V}_c} \sum_{f \in C} F_f, \tag{38}$$

which is monotonic if (29) and (30) are used as bounds on ψ. Alternatively, global bounds such as $\left[\psi_{\min}, \psi_{\max}\right] = \left[0, 1\right]$ can be specified.

3 | ADVECTION TEST CASES

3.1 | One-dimensional Advection

The first test of the adaptively implicit MPDATA is one dimensional with uniform velocity. Variable resolution is used so that the Courant number varies in space and implicit time stepping is used only where resolution is coarse. The variable resolution grids have resolution a factor of R finer in the middle of the unit length domain than the end points. There are n cells ($n+1$ grid points) in the unit length and a constant ratio, $r = R^{\frac{2}{n-2}}$, between successive cells in the first half of the domain and $\frac{1}{r}$ in the second half. Therefore the resolution of cell i is:

$$\Delta x_i = \begin{cases} \frac{1}{2} R r^{-i} \frac{1-r}{1-rR} & i \leq \frac{n}{2} - 1 \\ \frac{1}{2} R r^{\frac{n}{2}-i} \frac{1-r}{1-rR} & i \geq \frac{n}{2}. \end{cases} \tag{39}$$

We use smooth initial conditions for evaluating convergence with resolution and mixed initial conditions for inspecting boundedness and overall quality of solution:

$$\psi^0_{\text{smooth}} = \begin{cases} \frac{1}{2}\left\{1 + \cos \pi \left(4x - 1\right)\right\} & x \in \left[0, 0.5\right] \\ 0 & \text{otherwise,} \end{cases} \tag{40}$$

$$\psi^0_{\text{mixed}} = \begin{cases} \frac{1}{2}\left\{1 + \cos \pi \left(4x - 1\right)\right\} & x \in \left[0, 0.5\right] \\ 1 & x \in \left[0.6, 0.8\right] \\ 0 & \text{otherwise.} \end{cases} \tag{41}$$

All simulations use a velocity of $u = 1$ and run for one time unit so that the tracer travels one complete revolution around the periodic domain.

Fig. 3 shows solutions starting from the mixed initial conditions using 100 time steps each of length $\Delta t = 0.01$. The uniform resolution has 40 cells giving a uniform Courant number of 0.4 (meaning that the time stepping is purely explicit). The non-uniform resolution has 100 cells with $R = 10$ giving a Courant numbers in the range $c \in \left[0.4, 4\right]$ so that implicit time stepping is used where $c > 0.75$. As expected, the MPDATA results (top row of Fig. 3) are always

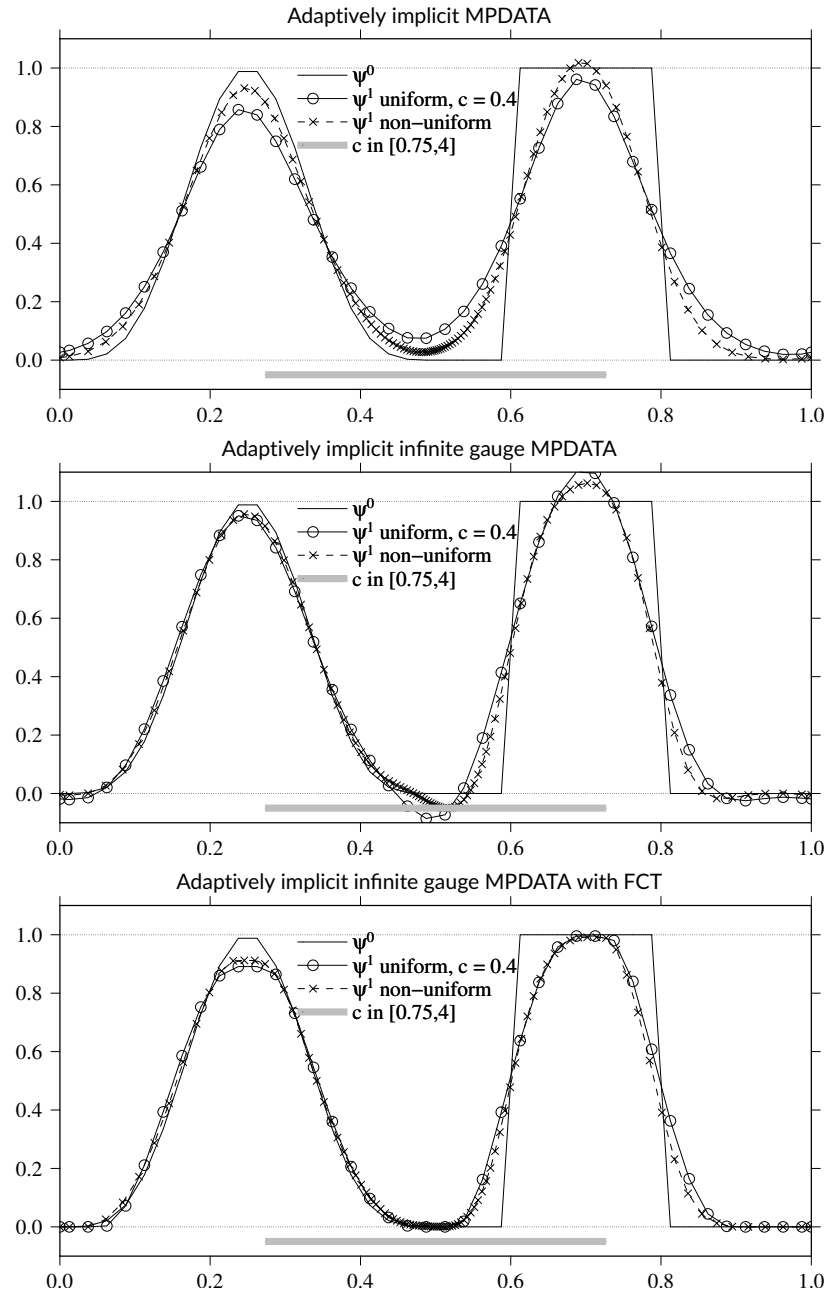

FIGURE 3 Advection once around a periodic domain starting from mixed initial conditions, ψ^0, using 40 grid points for the uniform resolution and 100 grid points for the resolution with a factor $R = 10$ between finest and coarsest. The regions where the non-uniform resolution has a Courant number greater than 0.75 (where implicit time stepping is used) is shaded grey.

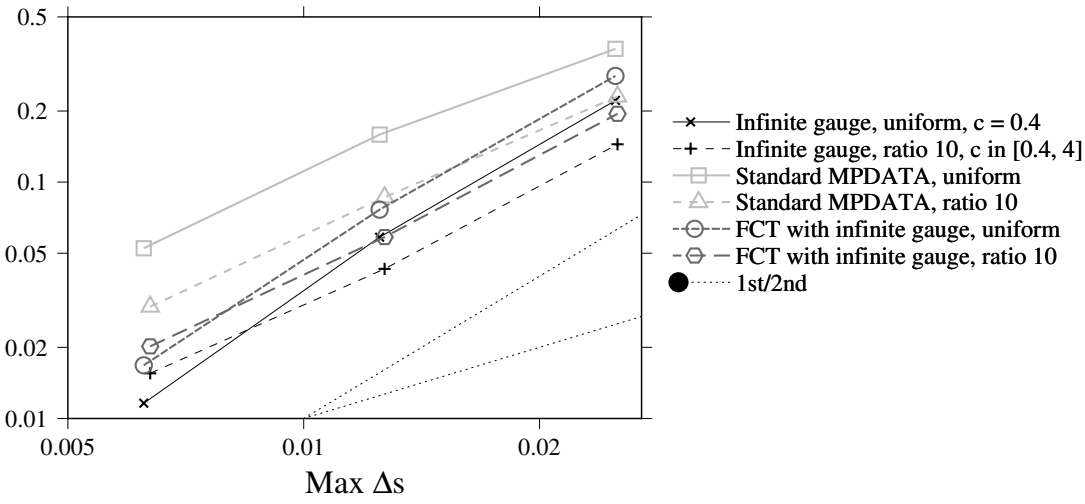

FIGURE 4 Convergence of the ℓ_2 error norm with resolution of the one-dimensional advection of the smooth initial conditions, ψ^0. The uniform resolutions use 20, 40 and 80 grid points and the non-uniform resolutions use 50, 100 and 200 grid points with ratio $R = 10$. Both use time steps of $\Delta t = 0.02$, 0.01 and 0.005. Dotted lines show the slope of first and second-order convergence.

positive for both the uniform resolution (explicit time stepping) and the non-uniform resolution (adaptively implicit). The non-uniform resolution produces a stable overshoot above the square wave which can happen with MPDATA without limited fluxes. The infinite gauge version (middle row of Fig. 3) produces undershoots and overshoots and the solution is more accurate in the region of the smooth wave. Neither the uniform (explicit) or non-uniform (adaptively implicit) results appear more accurate than the other although more grid points are used for the variable resolution. The infinite gauge results using FCT (bottom row of Fig. 3) are bounded, demonstrating the correct application of the flux corrections applied to adaptively implicit time stepping. The uniform (explicit) or non-uniform (adaptively implicit) results appear similar.

Convergence with resolution for all schemes on uniform and non-uniform meshes starting from the smooth initial conditions is shown in Fig. 4. The time step is scaled with the resolution so that the uniform meshes retain $c = 0.4$ at all resolutions and the non-uniform meshes retain $c \in [0.4, 4]$. The standard and infinite-gauge MPDATA with and without FCT give second-order convergence. Even though the non-uniform grid means that the Courant number reaches 4 at the centre of the domain, the convergence remains strong.

3.2 | Spherical Meshes

Advection test cases using adaptively implicit MPDATA calculated using various meshes are presented. There is no clearly optimal mesh of the sphere for atmospheric modelling (example meshes in Fig. 5). Numerical methods need to be designed to allow for one or more of the following features of meshes of the sphere:

1. Latitude-longitude meshes are orthogonal and have uniform resolution following co-ordinate lines but they have severe convergence of mesh lines towards two poles so numerical methods are needed that can cope with very

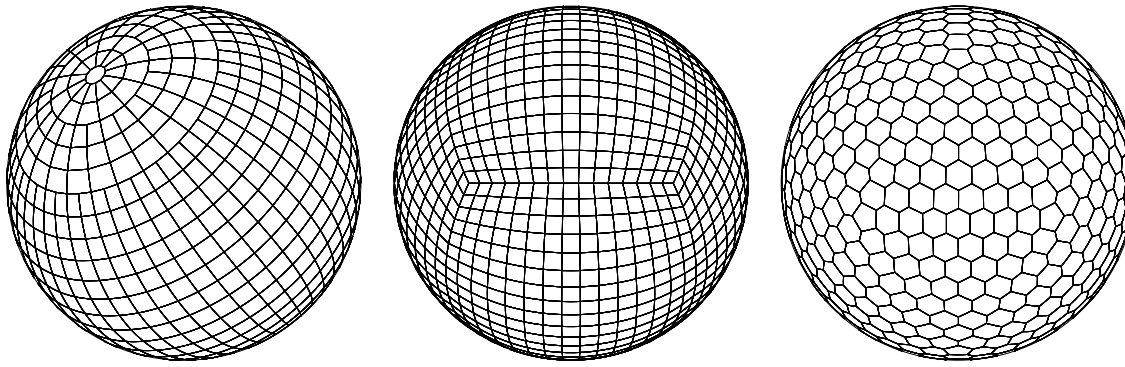

FIGURE 5 Some common meshes of the sphere viewed from above a point at a latitude of 45^o.

large Courant numbers. We use a latitude-longitude mesh with a cell at each pole (Fig. 5).

2. Hexagonal and triangular meshes of the sphere are quasi-uniform but they cannot be all three of:
   a. orthogonal (mesh lines and cell centre to cell centre lines cross at right angles)
   b. centroidal (cell centres are at cell centroids)
   c. non-skew (cell centre to cell centre lines bisect mesh lines)

   meaning that special numerical treatment is needed in order to achieve second-order accuracy.
3. Quasi-uniform versions of the cubed-sphere are non-orthogonal with large distortions (skewness) at cube edges and corners so numerical methods are needed that maintain accuracy at these distortions. The cubed-sphere in Fig. 5 uses the Gnomonic projection (Rančić et al., 1996).
4. Skipped latitude-longitude meshes have factor of two reductions in resolution in the longitudinal direction at a few latitudes to prevent the mesh lines converging. At latitudes where the resolution reduces, the meshes can be treated as non-conforming so that two quadrilateral cells are connected to one edge of the adjacent quadrilateral cell, or conforming with two quadrilaterals connected to adjacent, aligned edges of a distorted pentagon. The implementation described here treats them as conforming.

All of the meshes were decomposed into four domains for parallel processing with MPI.

3.3 | Deformational Flow

Lauritzen et al. (2012) describe deformational flow test cases to demonstrate a number of numerical properties of an advection scheme including order of convergence and monotonicity. We are using the non-divergent wind field which deforms and translates the initial conditions so that the final solution ($t = T = 5$) should be identical to the initial conditions ($t = 0$). The wind is defined by a stream function, Ψ, based on latitude, ϕ, longitude, λ, time, t and the radius of the sphere, $R = 1$:

$$\Psi\left(\lambda, \phi, t\right) = \frac{10R}{T} \sin^2\left(\lambda - \frac{2\pi t}{T}\right) \cos^2\phi \cos\frac{\pi t}{T} - \frac{2\pi R}{T} \sin\phi. \tag{42}$$

Mesh type	Nominal	N. cells	Δs	Δt	Figure
Latitude-longitude	120×60	7,080	3.0^o	0.02	7c, 8b
	240×120	28,800	1.5^o	0.01	6, 7, 8
	480×240	114,720	0.75^o	0.005	7c, 8b,9
Skipped latitude-	48×24	864	7.5^o		5
	120×60	5,310	3.0^o	0.02	7c, 8b
longitude	240×120	21,750	1.5^o	0.01	6, 7, 8
	480×240	88,470	0.75^o	0.005	7c, 8b,9
Cubed-sphere	$15 \times 15 \times 6$	1,350	6.4^o		5
	$30 \times 30 \times 6$	5,400	3.2^o	0.02	7c, 8b
	$60 \times 60 \times 6$	21,600	1.6^o	0.01	6, 7, 8
	$120 \times 120 \times 6$	86,400	0.8^o	0.005	7c, 8b,9
Hexagonal-	HR4	642	9.5^o		5
	HR6	10,242	2.4^o	0.02	7c, 8b
icosahedral	HR7	40,962	1.2^o	0.01	6, 7, 8
	HR8	163,842	0.6^o	0.005	7c, 8b,9

TABLE 1 Resolutions and time steps for deformational advection. Δs is a typical cell centre to cell centre distance in degrees latitude.

3.3.1 | Gaussian Hills

The Gaussian hills initial conditions are smooth and so can be used to measure the numerical order of convergence. The initial conditions of the tracer, ψ_0, are given in terms of the three dimensional position vector, $\mathbf{x}$, in Cartesian co-ordinates:

$$\psi_0(\mathbf{x}) = 0.95\left[\exp\left\{-5\left(\mathbf{x}-\mathbf{x}_1\right)^2\right\}+\exp\left\{-5\left(\mathbf{x}-\mathbf{x}_2\right)^2\right\}\right], \tag{43}$$

$$\text{where } \mathbf{x}_i = \left(R\cos\phi_i\cos\lambda_i,\ R\cos\phi_i\sin\lambda_i,\ R\sin\phi_i\right), \tag{44}$$

$$\left(\lambda_1,\phi_1\right) = \left(5\pi 6,\ 0\right) \tag{45}$$

$$\left(\lambda_2,\phi_2\right) = \left(7\pi 6,\ 0\right). \tag{46}$$

The tracer concentrations at $t = 2.5$ are shown in Fig. 6 calculated on five different meshes of the sphere and for a 30^o rotated version of the latitude-longitude mesh, all at a similar resolution. These use the standard adaptively implicit MPDATA without FCT.

Simulations using all the meshes in Fig. 6 use a time step of 0.01 (500 time steps in total) giving a Courant number

of around 2 so that the simulations would be unstable if a purely explicit scheme were used. Results on the rotated latitude-longitude mesh with a time step of 0.05 are also shown, leading to a maximum Courant number of around 10. Courant numbers at $t = 0$ are contoured in Fig. 6. Spatial resolutions and time steps are shown in table 1.

The flow goes to zero at the north and south poles so the convergence of meridians of the un-rotated latitude-longitude mesh does not lead to large Courant numbers. However when the mesh is rotated by 30^o, high winds cross the poles of the mesh so the maximum Courant number goes up to 70 (the contours in Fig. 6 show the Courant number at $t = 0$). These large Courant numbers do not lead to instability, a lack of sign-preservation or visible artefacts in the solution. The largest Courant numbers are removed on the rotated, skipped latitude longitude mesh although Courant numbers above 2 are present at $t = 0$, just poleward of the change in longitudinal resolution. On the cubed-sphere, the Courant number is largest near the cube corners due to mesh distortions and smaller cells. Some mesh imprinting is visible along the cube edges although this does not lead to a lack of sign-preservation. The hexagonal icosahedral meshes are the most uniform meshes of the sphere and so there are no sharp spikes in the Courant number. The results from the hexagonal mesh appear accurate but note that this mesh has higher resolution than the other meshes. The solutions using a larger time step on a full latitude longitude mesh have severely degraded accuracy with the Courant number being large over most of the domain and so very little of the high order MPDATA correction can be applied.

MPDATA is, by design, sign-preserving but not monotonic. The adaptively implicit MPDATA retains this feature on all of the meshes tested and displayed in Fig. 6. The minimum and maximum tracer values for all time steps for each of the meshes in Fig. 6 are shown at the top of Fig. 7. All of the minima remain positive and very close to zero. The maxima decrease due to numerical diffusion but they do not decrease monotonically, as expected using the standard MPDATA.

The maximum and mean Courant number for each time step for each of the meshes in Fig. 6 are shown in the middle row of Fig. 7. The maximum Courant number for all meshes is greater than one using the time step of 0.01 and is minimum at the middle of the simulation ($t = 2.5$). The maximum Courant number for the rotated latitude-longitude mesh reaches 70 and is always much larger than one which does not appear to significantly reduce the accuracy. The mean Courant numbers (dashed) are below or close to one throughout which helps to maintain accuracy apart from for the simulation with a larger time step.

The convergence of the ℓ_2 error norm with resolution is shown in the bottom row of Fig. 7. The mesh resolutions and time steps for these simulations are given in table 1. The resolution to time step ratio is kept constant along each line. Included in this graph are simulations using half the time step and five times the time step for the latitude-longitude mesh (giving maximum Courant number around one and around ten) in order show the impact of varying the mean Courant number. Reducing the time step to get $c < 1$ means that the standard explicit MPDATA is used almost everywhere. This increases the error slightly, which can be expected given the smooth flow. When the Courant number is close to 2, θ is close to $\frac{1}{2}$ and the temporal error correction is small. This implies that using second-order adaptively implicit time stepping is more accurate than using first-order time stepping with a correction. However the adaptively implicit time stepping requires a matrix inversion and so is more expensive. The simulation with $c \leq 10$ is much less accurate because the temporal correction is not applied for $c \geq 2$. However the simulation is still stable and sign preserving.

The convergence with resolution in Fig. 7 is around first-order at coarse resolution and approaches second-order at higher resolution, as expected for a second-order schemes (the asymptotic convergence is second order). The errors in Fig. 7 are similar to the second-order schemes presented in Lauritzen et al. (2014).

Better accuracy at the expense of sign-preservation can be achieved with the infinite gauge variant of MPDATA (a realisation of Lax-Wendroff) which works for the adaptively implicit version in the same way as the standard MPDATA (Smolarkiewicz and Clark, 1986). The maximum and minimum values of the tracer for infinite gauge simulations with

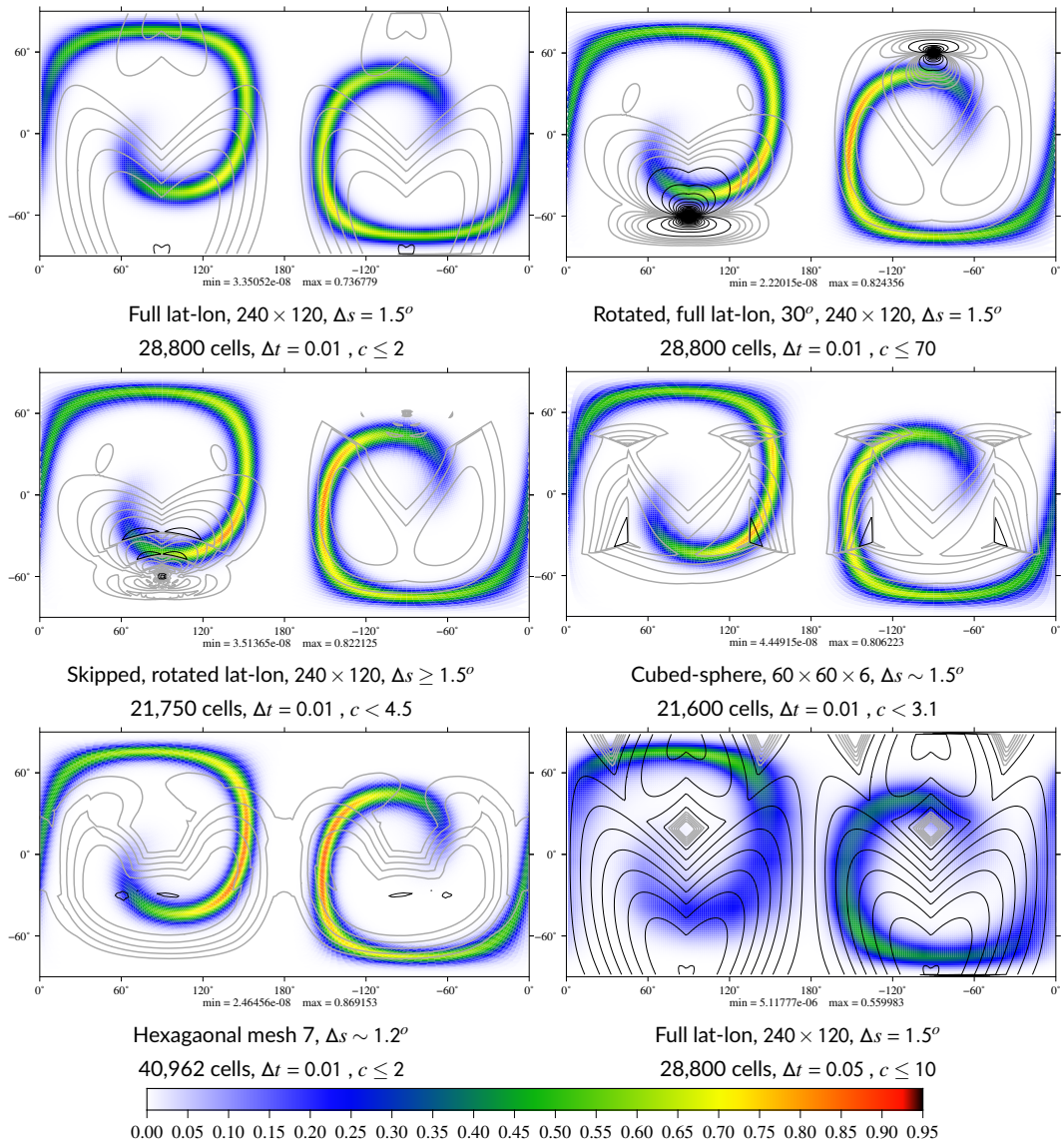

FIGURE 6 Deformational flow on the sphere. The colours show the tracer at $t = 1.5$ (piece-wise constant in each cell). The grey contours show the Courant number at $t = 0$ from 0.8 to 1.8 every 0.2 and the black contours are from 2 to 50 every 1.

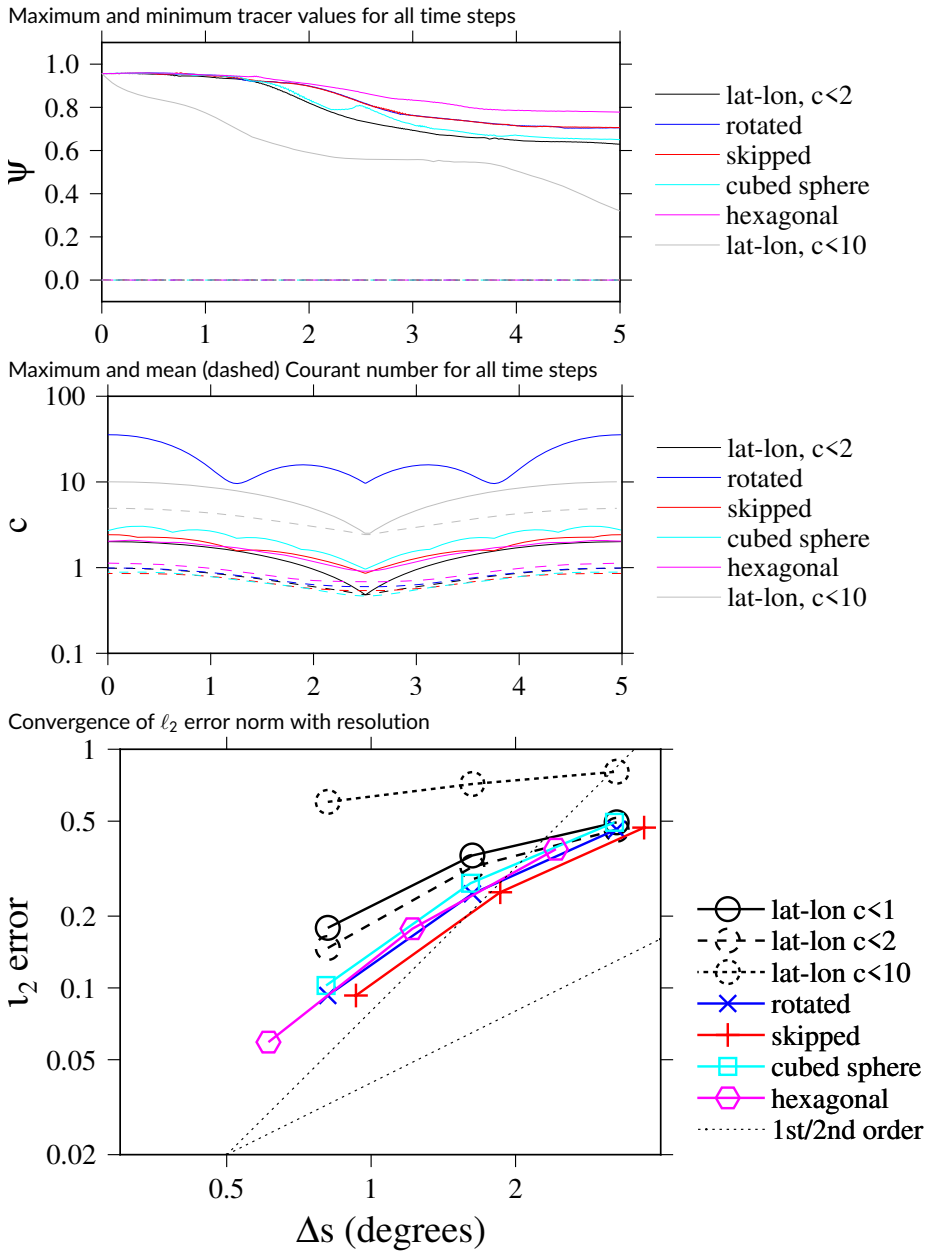

FIGURE 7 Diagnostics of the results for the deformational flow of the Gaussian hills with standard adaptively implicit MPDATA without FCT. Top and middle are diagnostics of the simulations shown in Fig. 6. Bottom includes other resolutions. Mesh and time step details in table 1.

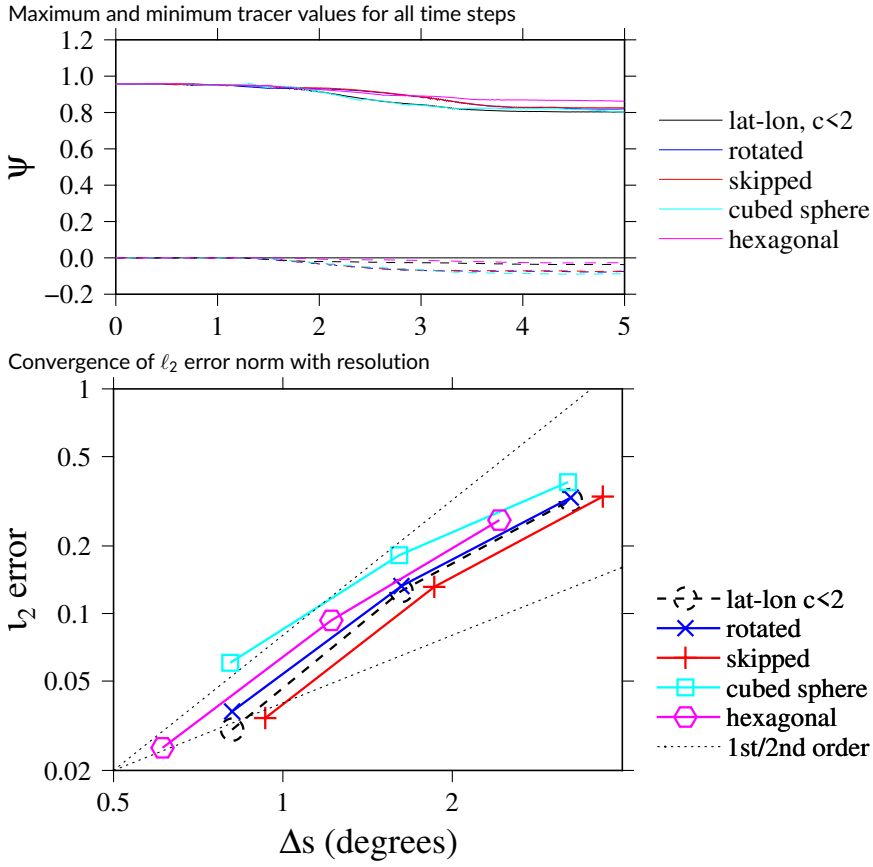

FIGURE 8 Diagnostics of the results for the deformational flow of the Gaussian hills with adaptively implicit infinite gauge MPDATA without FCT. Other settings the same as Fig. 7.

the same resolution as those shown in Fig. 6 are shown in Fig. 8. In comparison to the standard MPDATA simulations (Fig. 7) the infinite gauge results have a smaller reduction in the maximum (because the results are more accurate and hence less diffusive) but the minima is less than zero (spurious undershoots are generated). ℓ_2 errors with resolution are shown at the bottom of Fig. 8. The mesh spacing and times steps are the same as in Fig. 7 and are shown in table 1 . The order of convergence is higher and the ℓ_2 errors lower than standard MPDATA results (Fig. 7).

3.3.2 | Slotted Cylinders

Deformational advection of slotted cylinders tests the implementation of limiters. Lauritzen et al. (2012) recommend the same deformational velocity field as for the Gaussian hills with initial tracers defined by:

$$\psi_0\left(\lambda,\phi\right) = \begin{cases} 1 & \text{if } r_i \leq r \text{ and } |\lambda-\lambda_i| \geq \frac{r}{6R} \text{ for } i=1,2 \\ 1 & \text{if } r_1 \leq r \text{ and } |\lambda-\lambda_1| < \frac{r}{6R} \text{ and } \phi-\phi_1 < -\frac{5}{12}\frac{r}{R} \\ 1 & \text{if } r_2 \leq r \text{ and } |\lambda-\lambda_2| < \frac{r}{6R} \text{ and } \phi-\phi_2 > \frac{5}{12}\frac{r}{R}, \\ 0.1 & \text{otherwise} \end{cases} \tag{47}$$

$$\text{where } \mathbf{x} = \left(R\cos\phi\cos\lambda,\ R\cos\phi\sin\lambda,\ R\sin\phi\right) \tag{48}$$

$$r = R2,\ r_i = |\mathbf{x}-\mathbf{x}_i| \tag{49}$$

$$\left(\lambda_1,\phi_1\right) = \left(5\pi 6,\ 0\right) \tag{50}$$

$$\left(\lambda_2,\phi_2\right) = \left(7\pi 6,\ 0\right). \tag{51}$$

The tracer fields at the end of the simulations ($t = T = 5$) are shown in Fig. 9 for all meshes at the highest resolution used and at time steps giving Courant numbers of around 2 (see table 1). This uses the adaptively implicit infinite gauge MPDATA with FCT (limited to ensure monotonicity). Fig. 9 shows that the bounds of the initial conditions are maintained and no new extrema are generated, even on the rotated latitude-longitude mesh where the Courant number reaches 140. The skipped latitude-longitude mesh has sharp jumps in the Courant number (shown at $t = 5$) which do not cause artefacts in the solution. This is, to our knowledge, the first monotonic and conservative solution of the advection equation using such a large Courant number.

A simulation using the much larger time step which give a maximum Courant number of 10 on the unrotated latitude-longitude mesh is also shown in Fig. 9. Monotonicity is preserved but the solution loses accuracy at this globally large Courant number as the MPDATA correction cannot be applied in full for $c > 2$.

3.4 | Solver Performance

Solver performance is reported for a selection of simulations using full latitude-longitude meshes as the large inhomogeneity of cell size and large range of Courant numbers could lead to an ill conditioned matrix and poor solver performance (Tumolo and Bonaventura, 2015). These are compared with solver performance on the highest resolution hexagonal mesh. Each time step consists of one implicit solve using the standard OpenFOAM bi-conjugate gradient solver with a diagonal-based incomplete LU preconditioner. The solver tolerance is

$$\frac{\mathscr{V}_c|\mathbf{y}-A\mathbf{x}|}{\mathscr{V}_c\left(|\mathbf{y}|-|A\mathbf{x}|\right)}, \tag{52}$$

for matrix equation $A\mathbf{x} = \mathbf{y}$ where the sum is over all cells of the mesh and $\mathscr{V}_c$ is the cell volume. A tolerance of 10^{-6} is used for all simulations. The first guess of the solver is the state at the previous time step so the initial residual is small for small time steps.

The number of iterations of the solver per time step is shown in Fig. 10 for various resolutions and various time steps both rotated and unrotated on the latitude-longitude mesh and on the hexagonal mesh. The number of iterations is smallest around time 2.5 when the wind speed is lowest and so the Courant number is smallest. For simulations

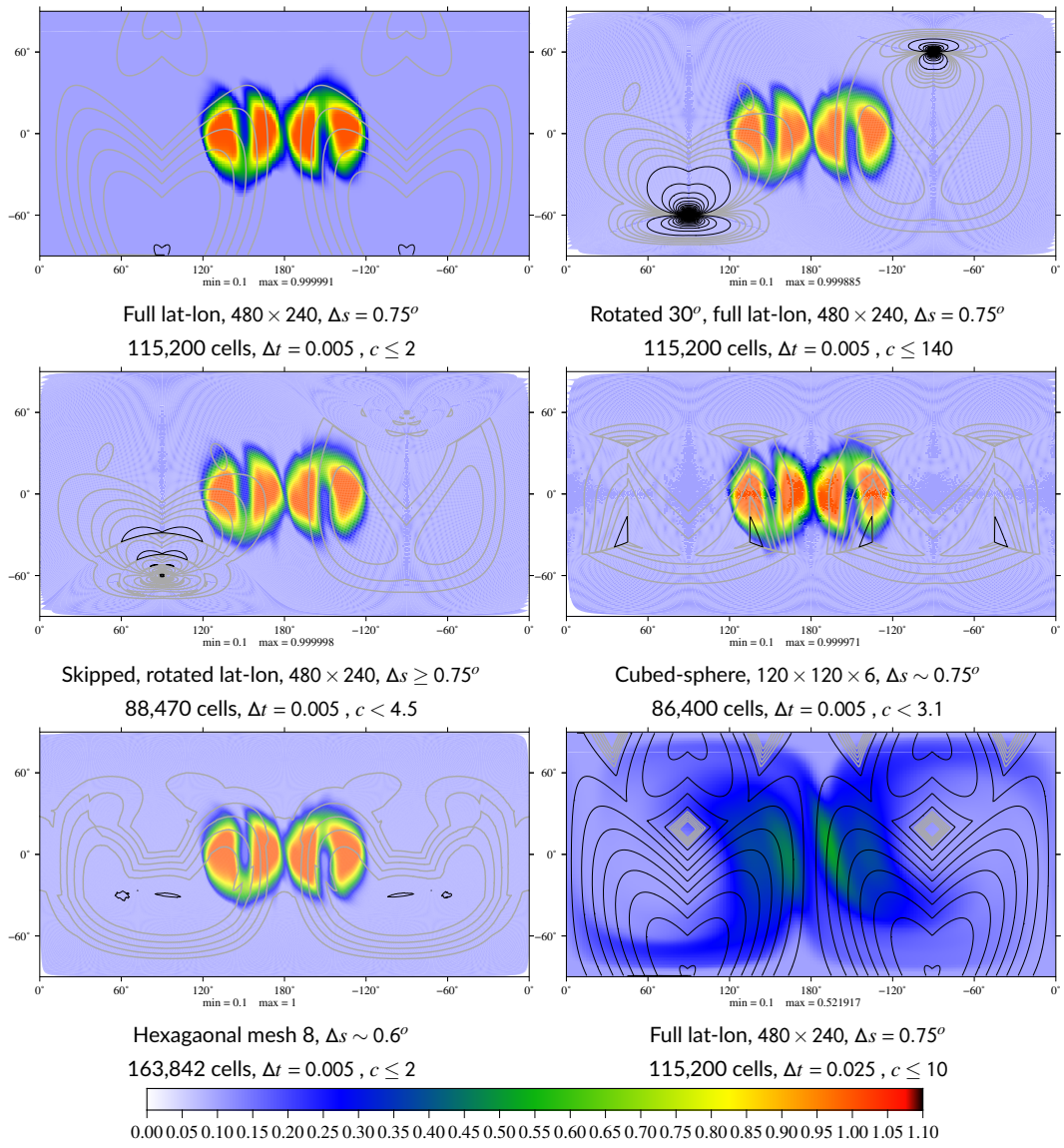

FIGURE 9 Deformational flow on the sphere after 5 time units. The colours show the piecewise uniform value of the tracer value in each cell. The grey contours show the Courant number from 0.8 to 1.8 every 0.2 and the black contours are from 2 to 50 every 1.

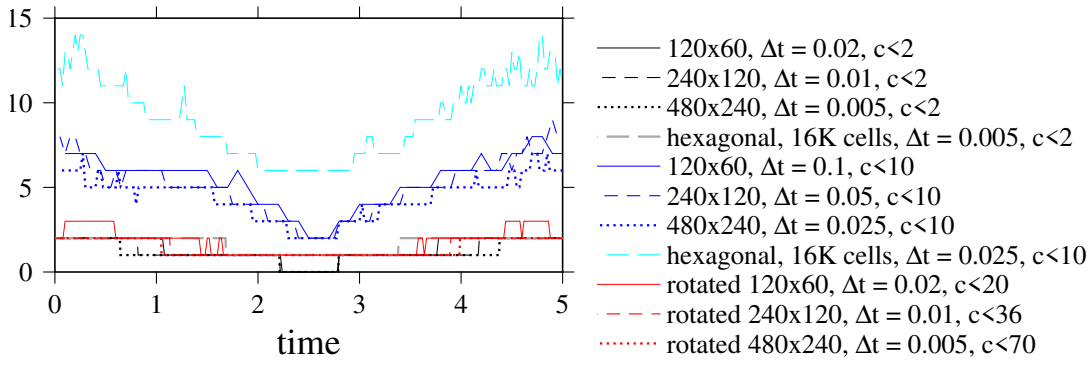

FIGURE 10 Number of solver iterations per time step for simulations on full latitude-longitude meshes and the highest resolution hexagonal mesh.

with the maximum Courant number less than 0.75 in the middle of the simulations, the number of solver iterations drops to zero because the simulation is purely explicit. The simulations represented by black and grey lines have a maximum Courant number of 2 and so the number of iterations is small throughout the simulation. The simulations where the maximum Courant number reaches 10 (in blue) use more iterations but for the latitude-longitude mesh, the number of iterations increases slower than linearly with Courant number, which is necessary for efficiency. However the hexagonal mesh with a maximum Courant number of 10 uses more than 5 times as many solver iterations as with a maximum Courant number of 2. This could be because the matrix solver is unsuitable for the reduced sparsity of the hexagonal mesh. The hexagonal mesh has nearly uniform global resolution and so the Courant number is high globally. This setup also leads to low accuracy, demonstrating the futility using implicit methods to achieve large time steps if the Courant number is high everywhere.

The rotated latitude-longitude meshes have very high maximum Courant numbers but only in limited regions. The residual is a volume average over the whole mesh so the higher errors near the mesh poles do not prevent global convergence but are still being solved accurately enough to prevent instability around the pole. Therefore the rotated mesh simulations do not have high iteration counts for any of the resolutions tested and the accuracy is high. It should be noted that implicit solutions in limited regions will lead to load balancing problems. Therefore if it is known in advance that some regions are more likely to need implicit solves, then smaller domains could be used there.

It should also be noted that higher spatial resolution has little influence on the number of iterations per time step for all mesh types and Courant numbers, which is encouraging.

4 | SUMMARY AND CONCLUSIONS

This paper has shown how MPDATA can be extended for adaptively implicit time-stepping, enabling Courant numbers much larger than one. Two dimensional deformational flow advection test cases on the sphere show that solutions are accurate with Courant numbers above one over a large fraction of the domain and accurate with local Courant number spikes over 100, such as happen over the pole of a latitude-longitude mesh. There are a number of novel aspects to the paper and the advection scheme presented:

1. An adaptively implicit version of finite-volume MPDATA which is stable for arbitrary Courant numbers and on

arbitrary meshes.

2. Transport over the poles of a latitude-longitude mesh at high wind speed without reductions in accuracy or increased cost.
3. Monotonicity for all Courant numbers by adapting FCT (Zalesak, 1979) for implicit time stepping.
4. Accuracy of the adaptively implicit scheme for modest Courant numbers (up to two) and first-order accuracy as Courant numbers grow beyond 2.
5. A proof that the adaptively implicit time stepping, in combination with first-order upwind spatial discretisation, is bounded.
6. A demonstration of the advection scheme on a variety of meshes of the sphere.
7. A first look at solver performance which shows that iteration count increases slower than linearly with Courant number, implying that computational speed can be gained from larger time steps (the exception to this is on the hexagonal mesh).

This paper goes further than recent papers presenting advection schemes that are adaptively implicit in the vertical only (Wicker and Skamarock, 2020; Li and Zhang, 2022), not only in the use of implicit time stepping in two dimensions but also improved accuracy while using implicit time stepping and a proof that the mix of implicit and explicit does not destroy boundedness.

The introduction described multi-tracer efficiency as an essential property of an advection scheme. Using implicit time-stepping, a separate solver for each tracer would be necessary, which initially sounds prohibitive. However, much of the cost of an implicit solve is in preconditioning, which would be shared over all tracers which use the same wind field.

Next steps entail three-dimensional solutions and incorporation into a full dynamical core with implicit time stepping for advection in all equations.

Acknowledgements

references

Baldauf, M., Seifert, A., Förstner, J., Majewski, D., Raschendorfer, M. and Reinhardt, T. (2011) Operational convective-scale numerical weather prediction with the COSMO model: Description and sensitivities. *Mon. Wea. Rev.*, **139**, 3887–3905.

Chen, Y., Weller, H., Pring, S. and Shaw, J. (2017) Comparison of dimensionally split and multi-dimensional atmospheric transport schemes for long time steps. *Q. J. R. Meteorol. Soc.*, **143**, 2764–2779.

Cullen, M. and Davies, T. (1991) A conservative split-explicit integration scheme with fourth-order horizontal advection. *Q. J. R. Meteorol. Soc.*, **117**, 993–1002.

Davies, T., Cullen, M., Malcolm, A., Mawson, M., Staniforth, A., White, A. and Wood, N. (2005) A new dynamical core for the Met Office's global and regional modelling of the atmosphere. *Q. J. R. Meteorol. Soc.*, **131**, 1759–1782.

Gottlieb, S., Shu, C.-W. and Tadmor, E. (2001) Strong stability-preserving high-order time discretization methods. *SIAM review*, **43**, 89–112.

Harris, L. M., Lauritzen, P. H. and Mittal, R. (2011) A flux-form version of the conservative semi-lagrangian multi-tracer transport scheme (CSLAM) on the cubed sphere grid. *J. Comput. Phys.*, **230**, 1215–1237.

Hirt, C., Amsden, A. and Cook, J. (1997) An arbitrary Lagrangian-Eulerian computing method for all flow speeds. *J. Comput. Phys.*, **135**, 203–216. URL: `http://www.sciencedirect.com/science/article/pii/S0021999197957028`.

Jebens, S., Knoth, O. and Weiner, R. (2011) Partially implicit peer methods for the compressible Euler equations. *J. Comput. Phys.*

Kühnlein, C., Deconinck, W., Klein, R., Malardel, S., Piotrowski, Z. P., Smolarkiewicz, P. K., Szmelter, J. and Wedi, N. P. (2019) FVM 1.0: a nonhydrostatic finite-volume dynamical core for the IFS. *Geosci. Model Dev.*, **12**, 651–676.

Kühnlein, C. and Smolarkiewicz, P. K. (2017) An unstructured-mesh finite-volume MPDATA for compressible atmospheric dynamics. *J. Comput. Phys.*, **334**, 16–30.

Lauritzen, P., Skamarock, W., Prather, M. and Taylor, M. (2012) A standard test case suite for two-dimensional linear transport on the sphere. *Geosci. Model Dev.*, **5**, 887–901.

Lauritzen, P., Ullrich, P., Jablonowski, C., Bosler, P., Calhoun, D., Conley, A., Enomoto, T., Dong, L., Dubey, S., Guba, O., Hansen, A., Kaas, E., Kent, J., Lamarque, J.-F., Prather, M., Reinert, D., Shashkin, V., Skamarock, W., Sørensen, B., Taylor, M. and Tolstykh, M. (2014) A standard test case suite for two-dimensional linear transport on the sphere: results from a collection of state-of-the-art schemes. *Geosci. Model Dev.*, **7**, 105–145.

Leonard, B., Lock, A. and MacVean, M. (1996) Conservative explicit unrestricted-time-step multidimensional constancy-preserving advection schemes. *Mon. Wea. Rev.*, **124**, 2585–2606.

Li, J. and Zhang, Y. (2022) Enhancing the stability of a global model by using an adaptively implicit vertical moist transport scheme. *Meteorol Atmos Phys*, **134**.

Lin, S.-J. (2004) A "vertically Lagrangian" finite-volume dynamical core for global models. *Mon. Wea. Rev.*, **132**, 2293–2307.

May, S. and Berger, M. (2017) An explicit implicit scheme for cut cells in embedded boundary meshes. *J. Comput. Phys.*

Miura, H. (2007) An upwind-biased conservative advection scheme for spherical hexagonal-pentagonal grids. *Mon. Wea. Rev.*, **135**, 4038–4044.

Rančić, M., Purser, R. and Mesinger, F. (1996) A global shallow-water model using an expanded spherical cube: Gnomonic versus conformal coordinates. *Q. J. R. Meteorol. Soc.*, **122**, 959–982.

Smolarkiewicz, P. (1983) A simple positive definite advection scheme with small implicit diffusion. *Mon. Wea. Rev.*, **111**, 479–486.

— (1984) A fully multidimensional positive definite advection transport algorithm with small implicit diffusion. *J. Comput. Phys.*, **54**, 325–362.

Smolarkiewicz, P. and Clark, T. (1986) The multidimensional positive definite advection transport algorithm: Further development and applications. *J. Comput. Phys.*, **67**, 396–438.

Smolarkiewicz, P. and Grabowski, W. (1990) The multidimensional positive definite advection transport algorithm: nonoscillatory option. *J. Comput. Phys.*, **86**, 355–375.

Smolarkiewicz, P. and Margolin, L. (1998) MPDATA: A finite-difference solver for geophysical flows. *J. Comput. Phys.*, **140**, 459–480.

Smolarkiewicz, P. and Szmelter, J. (2005) MPDATA: An edge-based unstructured-grid formulation. *J. Comput. Phys.*, **206**, 624–649.

Tumolo, G. and Bonaventura, L. (2015) A semi-implicit, semi-Lagrangian discontinuous Galerkin framework for adaptive numerical weather prediction. *Q. J. R. Meteorol. Soc.*, **141**, 2582–2601.

Ullrich, P. A., Jablonowski, C., Kent, J., Lauritzen, P. H., Nair, R., Reed, K. A., Zarzycki, C. M., Hall, D. M., Dazlich, D., Heikes, R., Konor, C., Randall, D., Dubos, T., Meurdesoif, Y., Chen, X., Harris, L., Kühnlein, C., Lee, V., Qaddouri, A., Girard, C., Giorgetta, M., Reinert, D., Klemp, J., Park, S.-H., Skamarock, W., Miura, H., Ohno, T., Yoshida, R., Walko, R., Reinecke, A. and Viner, K. (2017) DCMIP2016: a review of non-hydrostatic dynamical core design and intercomparison of participating models. *Geosci. Model Dev.*, **10**, 4477–4509.

Wicker, L. and Skamarock, W. (2020) An Implicit-Explicit Vertical Transport Scheme for Convection-Allowing Models. *Mon. Wea. Rev.*, **148**, 3893–3910.

Yee, H. (1987) Construction of explicit and implicit symmetric TVD schemes and their applications. *J. Comput. Phys.*, **68**, 151–179.

Yee, H., Warming, R. and Harten, A. (1985) Implicit total variation diminishing (TVD) schemes for steady-state calculations. *J. Comput. Phys.*, **57**, 327–360.

Zalesak, S. (1979) Fully multidimensional flux-corrected transport algorithms for fluids. *J. Comput. Phys.*, **31**, 335–362.

Zerroukat, M. and Allen, T. (2020) SLIC: A Semi-Lagrangian Implicitly Corrected method for solving the compressible Euler equations. *J. Comput. Phys.*, **421**, 109739.

A | BOUNDEDNESS OF THE FIRST-ORDER UPWIND ADAPTIVELY IMPLICIT SCHEME

The first-order upwind, adaptively implicit scheme can be written:

$$\begin{aligned}\psi_c^{n+1} = \psi_c^n \quad &+ \quad \frac{\Delta t}{\mathscr{V}_c}\sum_{i\in\mathsf{in}}\left(1-\theta_i\right)U_i\psi_i^n + \frac{\Delta t}{\mathscr{V}_c}\sum_{i\in\mathsf{in}}\theta_i U_i\psi_i^{n+1} \\ &- \quad \frac{\Delta t}{\mathscr{V}_c}\sum_{o\in\mathsf{out}}\left(1-\theta_o\right)U_o\psi_c^n - \frac{\Delta t}{\mathscr{V}_c}\sum_{o\in\mathsf{out}}\theta_o U_o\psi_c^{n+1},\end{aligned} \tag{53}$$

for cell C with faces i and o. Faces "$i \in$ in" have flow into cell C whereas faces "$o \in$ out" have flow out. Off centering values are denoted θ_i and θ_o at the different face types. $U_i \geq 0$ and $U_o > 0$ are the inward and outward fluxes. ψ_i are the values of ψ in cells through the i faces. The $\theta_{i,o}$ are defined on faces for conservation. This makes the boundedness of the scheme less straightforward. Eqn. (53) can be re-arranged to give:

$$\psi_c^{n+1} = \gamma\psi_c^n + \sum_{i\in\mathsf{in}}\alpha_i\psi_i^n + \sum_{i\in\mathsf{in}}\beta_i\psi_i^{n+1}, \tag{54}$$

where

$$\begin{aligned}\alpha_i &= \frac{\frac{\Delta t}{\mathscr{V}_c}\left(1-\theta_i\right)U_i}{1+\frac{\Delta t}{\mathscr{V}_c}\sum_{o\in\mathsf{out}}\theta_o U_o} \text{ for each } i \\ \beta_i &= \frac{\frac{\Delta t}{V_j}\theta_i U_i}{1+\frac{\Delta t}{\mathscr{V}_c}\sum_{o\in\mathsf{out}}\theta_o U_o} \text{ for each } i \\ \gamma &= \frac{1-\frac{\Delta t}{\mathscr{V}_c}\sum_{o\in\mathsf{out}}\left(1-\theta_o\right)U_o}{1+\frac{\Delta t}{\mathscr{V}_c}\sum_{o\in\mathsf{out}}\theta_o U_o}.\end{aligned}$$

The quantities α_i, β_i and γ are all positive as long as the θ_0 are chosen to give

$$\frac{\Delta t}{\mathscr{V}_c}_{o\in\text{out}}(1-\theta_o)\,U_o \leq 1, \tag{55}$$

which can be accomplished by setting

$$\theta_f \geq 1 - \frac{1}{\frac{\Delta t}{\mathscr{V}_c}_{o\in\text{out}} U_o}, \tag{56}$$

for the cells either side of face f. Hence all ψ are positive at the next time step. If, in addition the flow is discretely non-divergent then:

$$_{i\in\text{in}} U_i = _{o\in\text{out}} U_o, \tag{57}$$

which implies

$$_{i\in\text{in}} \alpha_i + _{i\in\text{in}} \beta_i + \gamma = 1, \tag{58}$$

so from Eqn. (54) ψ_c^{n+1} is a convex combination of ψ_c^n, ψ_i^n and ψ_i^{n+1}. This in fact proves that the scheme is globally bounded. This can be shown by contradiction; if we assume that ψ_c^{n+1} is the global maximum at t^{n+1} and it is greater than ψ_j^n for all cells j in the mesh then (54) and (58) cannot both hold for cell C. It is necessary for this scheme to be bounded as it is used as the bounded scheme for the FCT (section (2.5)).

B | STABILITY ANALYSIS OF THE SECOND-ORDER ADAPTIVELY IMPLICIT SCHEME

MPDATA is a non-linear scheme but the infinite gauge version is linear and so von-Neumman stability analysis can be applied. In one dimension, for constant velocity, $u > 0$, constant Δx, constant θ and constant Courant number $c = u\Delta t\Delta x$, the one-dimensional adaptively implicit scheme is

$$\begin{aligned} \psi_j^{n+1} &= \psi_j^n - c\,(1-\theta)\left(\psi_j^n - \psi_{j-1}^n\right) - c\theta\left(\psi_j^{n+1} - \psi_{j-1}^{n+1}\right) \\ &- \frac{c}{2}\left(1-\chi c\right)\left(\psi_{j+1}^n - 2\psi_j^n + \psi_{j-1}^n\right), \end{aligned} \tag{59}$$

where ψ_j is ψ at position $x = j\Delta x$. We showed in section (2.2) that $\chi = 1 - 2\theta$ gives second-order accuracy. From Appendix (A) we can see that we need $\theta \geq 1 - 1c$ for stability of the first-order upwind part (the first two terms of Eqn. (59)). In order to revert to the explicit version for $c \leq 1$ and to transition smoothly to the implicit version we use

$$\theta = \begin{cases} 0 & c \leq 1 \\ 1 - \frac{1}{c} & c > 1, \end{cases} \tag{60}$$

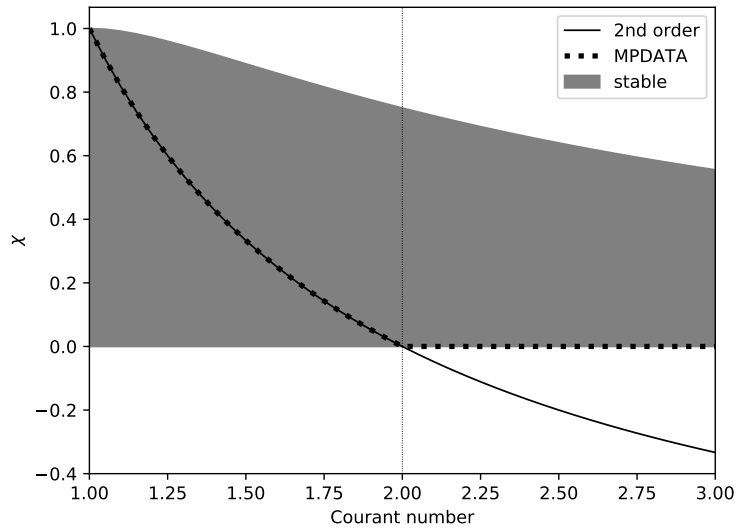

FIGURE 11 Comparison of the stability limits, the second-order requirement and the value of χ used for the MPDATA correction.

and analyse (59) separately for these two cases. Considering a Fourier mode with wavenumber k, the amplification factor, A, of (59) is

$$A = \frac{1 - c\left(\chi c - \theta\right)\left(1 - \cos k\Delta x\right) - ic\left(1 - \theta\right)\sin k\Delta x}{1 + c\theta\left(1 - \cos k\Delta x\right) + ic\theta \sin k\Delta x}. \tag{61}$$

For $\theta = 0$ and $\chi = 1$ we recover the usual Lax-Wendroff stability constraints of $c \in \left[-1, 1\right]$. For $c \geq 1$ and $\theta = 1 - \frac{1}{c}$ it can be shown that stability requires $\chi \in \left[0, \frac{2c-1}{c^2}\right]$. The stability range for χ is compared with the second-order requirement for χ in Fig. (11). For behaviour as close as possible to second-order for the maximum range of Courant numbers and for stability we use:

$$\chi = \max\left(1 - 2\theta,\ 0\right). \tag{62}$$

This gives an unconditionally stable scheme with second-order accuracy for $c \leq 2$.